The fight for a reactive site
Groot, I.M.N.

Chapter 6

Dynamics of dissociative adsorption of hydrogen on a CO-precovered Ru(0001) surface: A comparison of theoretical and experimental results

Abstract

We have studied hydrogen dissociation on a CO-precovered Ru(0001) surface, by means of six-dimensional (6D) quasi-classical and quantum dynamics. The 6D potential energy surface has been built by applying a modified Shepard interpolation method to a set of density functional theory (DFT) data, for a coverage of 1/3 monolayer CO. We compared our theoretical results to the experimental ones obtained by Ueta *et al.* [Chem. Phys. Chem. 9, 2372 (2008)]. In order to do so, we have simulated the supersonic molecular beam used in the experiments by taking into account the energy distribution and rovibrational states population in the molecular beam. We find that both the energy and rovibrational states distributions of the molecular beam influence the reactivity, with the largest effect being caused by the energy distribution. However, a significant discrepancy between theory and experiment persists. We argue that this discrepancy could be due to the RPBE functional used in the DFT calculations and/or the neglect of CO-motion in the calculations.

6.1 Introduction

The dissociative adsorption of H_2 on Ru(0001) can be considered as a model for gas-surface reactions with a relatively high reactivity. This process has been studied both experimentally [1], using supersonic molecular beam techniques, and theoretically, by using quantum dynamics calculations [2]. The experimental results [1] show an increasing reaction probability for increasing kinetic energy (direct dissociation over a wide distribution of barriers). In addition, they imply significant non-activated dissociation without a signature of steering or precursor-based mechanisms at low collision energies. The experiments also show that normal energy scaling is obeyed and that the reaction probability is independent of surface temperature (within the investigated range, 140-180 K). Moreover, no strong H_2/D_2 isotope effect is observed.

Calculations [2] performed for the same system, using two different functionals within the generalized gradient approximation (PW91 [3, 4] and RPBE [5]) predicted activated dissociation for both functionals with a narrower distribution of barriers than observed in experiment [1]. PW91 yields a more accurate minimum energy barrier than RPBE. When it comes to the overall agreement between theory and experiment, neither functional is better, PW91 producing the best results at low energies, and RPBE at high energies. Both functionals predict a reaction saturation value of 1 at kinetic energies above 0.25 eV (PW91) or 0.45 eV (RPBE), whereas the maximum reactivity measured in this energy range is 0.8.

The discrepancy found between theory and experiment could have several origins. First, phonons and electron-hole pair excitations could play a role in the experiments, but are ignored in the dynamical calculations. The presence of phonons is not expected to be of major importance, since the measured reaction probabilities seem to be independent of the surface temperature [1]. However, experiments could only be performed at a minimum surface temperature of 140 K. Cooling to lower temperatures takes a very long time and the surface becomes contaminated before the actual measurement is performed. Calculations, on the other hand, are performed for a frozen surface. At high kinetic energy (>0.35 eV), experiments show a constant reactivity independent of incidence kinetic energy. In principle, the experimental results could also be affected by electronic friction (*i.e.* electron-hole pair excitations), which are expected to be energy dependent and become more relevant for higher kinetic energies. However, the omission of e-h pair excitations in calculations has been justified and discussed in a recent work on reactive scattering of hydrogen from Pt(111) [6].

A second possible origin of the discrepancy between theory and experiment could be the energy distribution of the molecular beam. Especially at high nozzle temperatures, the Boltzmann distribution of the kinetic energy of the hydrogen molecules becomes fairly broad due to the incomplete cooling of the expansion. However, when convoluting the results of the calculations with measured energy distributions in the beam, a significant difference between theory and experiment persisted [1].

Third, the discrepancy at high kinetic energies could be caused by excited rotational states populated in the experiment. The rotational distribution in the molecular beam becomes broader at higher nozzle temperatures, whereas the theoretical study was done for $J = 0$ only. The rotational temperature of the molecular beam is 80% of the nozzle temperature [7–9]. This means that, even at room temperature, excited rotational states are present in the beam (for H$_2$ and $J = 0$, 1, 2, and 3, the populations are 16%, 70%, 9.3% and 4.7%, respectively [8]). At the highest nozzle temperature used (1700 K) states up to $J = 7$ are present (4.1%), with the majority of H$_2$ molecules present in the $J = 3$ state (30%). If excited rotational states would show lower reactivity than the rotational ground state, this could explain the lower reactivity observed at high kinetic energies when comparing experiment to theory.

To test the importance of taking into account the energy distribution of the molecular beam and the population of excited rotational and vibrational states in the beam for accurately simulating molecular beam reaction probabilities, we carried out a 6D quasi-classical and quantum dynamics study of hydrogen dissociative adsorption on a similar system, CO/Ru(0001), for which experimental results are available [10]. For a Ru(0001) surface precovered with 1/3 monolayer (ML) CO, we have built a 6D potential energy surface (PES) describing the electronic structure for the H$_2$ + CO/Ru(0001) interaction, and using this PES we have performed quantum and quasi-classical dynamics calculations. Here we present

initial-state-selected calculations for different rotational states (up to $J = 9$, for $v = 0$, and up to $J = 6$ for $v = 1$ for H$_2$, and up to $J = 15$ for $v = 0$ and 1 for D$_2$) for a range of kinetic energies relevant for molecular beam experiments. All possible values of m_J have been taken into account. In addition, we have convoluted the results for the rovibrational ground state calculations ($v = 0$, $J = 0$) with the energy distribution of the molecular beam used in the experiments [1, 10], and we show that this results only in small changes in the theoretical dynamics data for the system investigated. Finally, we show the results of a full molecular beam simulation (taking into account both the collision energy distribution and rovibrational state distributions of the beam) for both H$_2$ and D$_2$, and we compare the results with experiments [10].

   Another question we address is how well the frozen surface model for H$_2$ on metal surfaces covered with a layer of pre-adsorbed CO molecules performs. After relaxing the Ru slab with the CO molecule, we keep these atoms fixed at their relaxed positions. Since in experiments no surface temperature dependence is observed for the probed range (140-180 K), this seems justified. However, the incoming hydrogen molecule could cause the CO to move, an aspect that is not influenced by surface temperature, and thus could not be ruled out from the experiments.

   The rest of the paper is organized as follows. In Sec. 6.2 we describe the theoretical treatment applied to dynamics calculations: The 6D potential energy surface used, the quasi-classical and quantum dynamical methods, and the molecular beam simulation. Section 6.3 discusses the results of the calculations for different H$_2$/D$_2$ rotational states and compares reaction of H$_2$ in the vibrational ground state to that of H$_2$ in its first excited vibrational state. In addition, we present and discuss the convolution of the rovibrational ground state results with the energy distribution of the molecular beam and the averaging of the energy resolved reaction probability over the rovibrational states population, as well as the full beam simulation. Furthermore, we compare our results of the full molecular beam simulation to experimental data. Section 6.4 summarizes our main conclusions.

6.2   Theory

6.2.1   Potential energy surface

To investigate the dissociative adsorption of H$_2$ on the CO/Ru(0001) surface, we have built the 6D PES for the H$_2$ + CO/Ru(0001) system, by applying a modified Shepard (MS) interpolation method, initially developed for gas phase reactions [11–13] and adapted to gas-surface reactions [14]. The Ru atoms and the CO adsorbate were taken as frozen, after allowing the atoms to relax in the direction perpendicular to the surface. The fact that the reaction probability for hydrogen measured in experiments for H$_2$ + Ru(0001) [1] and for H$_2$ + CO/Ru(0001) [10] has been found to be independent of surface temperature, indicates that phonons are negligible and that therefore this approximation is reasonable. However, it is possible that CO moves to make room for the impinging H$_2$ molecules, something that cannot be ruled out from the experiments. Another approximation used is the Born-Oppenheimer approximation, *i.e.* neglecting electron-hole pair excitations [15]. As was noted before, the omission of e-h pair excitations in calculations has been justified and discussed in a recent work on reactive scattering of hydrogen from Pt(111) [6].
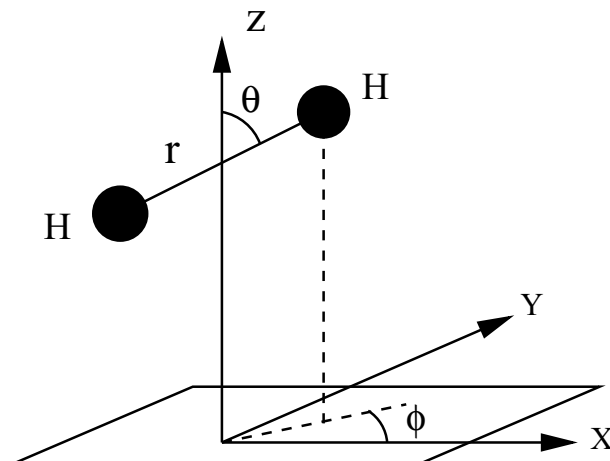
Figure 6.1: The six-dimensional $(X, Y, Z, r, \theta, \varphi)$ coordinate system used to describe the interaction of H_2 with the CO/Ru(0001) surface. For simplicity the CO molecules and Ru atoms are not explicitly shown.

H₂ + CO/Ru(0001) system

For carbon monoxide adsorbed on the Ru(0001) surface, a coverage of 1/3 ML was considered, with the CO molecules bound at the on-top sites, perpendicularly to the surface with the C atom closest to the Ru atoms. A $(\sqrt{3} \times \sqrt{3})$R30° surface unit cell was used, as this is the structure experimentally seen by LEED of 1/3 ML CO on Ru(0001) [16–19].

The H_2 molecular configuration was described by considering all six degrees of freedom $(X, Y, Z, r, \theta, \varphi)$. Here, r is the H-H distance, Z the distance from the center-of-mass of H_2 to the surface, X and Y represent the center-of-mass motion parallel to the surface, and θ and φ are the polar and azimuthal angles defining the orientation of the H-H molecular axis. $Z = 0$ corresponds to the average position in Z of the first layer Ru atoms (see Fig. 6.1). For further details concerning the unit cell used, we refer the reader to our previous publication (see Ref. [20] and Chapter 5 of this thesis).

Electronic structure calculations

The electronic structure calculations were done using DFT [21, 22] as implemented in the DACAPO code [23]. The exchange-correlation functional was described within the generalized gradient approximation (GGA), using the revised Perdew-Burke-Ernzerhof (RPBE) functional [5]. This functional is known to give rather accurate chemisorption energies for CO on several flat metal surfaces, including Ru(0001) [24]. In the case of dissociation of hydrogen on Ru(0001) neither the RPBE nor the PW91 functional yield chemical accuracy (43 meV) [1]. However, there is no systematic proof yet that other standard GGA functionals perform better for H_2-metal surface reactions. We selected the RPBE functional because it better describes the CO-Ru interaction and because it describes dissociation of H_2 on bare Ru(0001) equally well as the PW91 functional [1].

The ion cores were modeled by using ultrasoft pseudo-potentials and a plane-wave basis set was used for the electronic orbitals. A plane wave cut-off of 350 eV, a density cut-off of 700 eV, and (4,4,1) Monkhorst-Pack k-points were used to sample the Brillouin zone. For further details on modeling the CO/Ru(0001) system and the numerical parameters used in
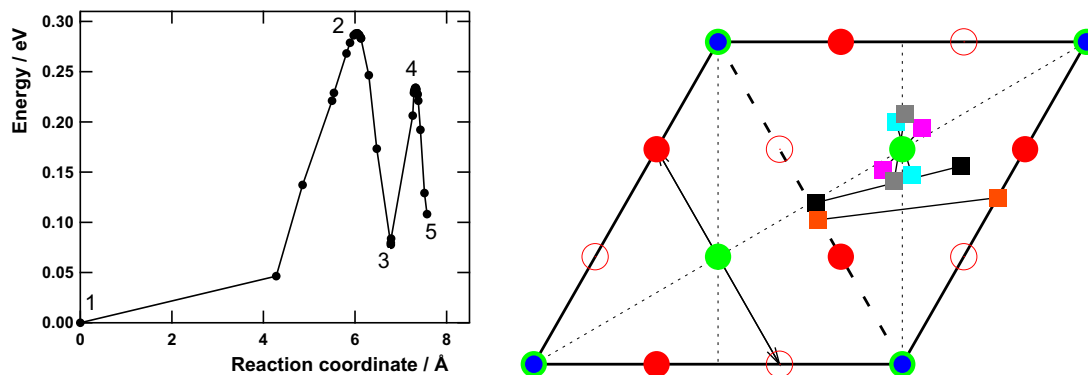
Figure 6.2: (Left panel) Energy versus reaction coordinate for one of the four reaction paths studied [20]. The energy of the gas phase is taken to be zero. (Right panel) For one of the four reaction paths studied [20] the positions of the hydrogen atoms in the initial state (pink), in the first barrier configuration (light blue), in the molecular chemisorption minimum (gray), in the second barrier configuration (black) and in the final state (orange) are shown in the CO/Ru(0001) unit cell. The dark blue circles represent CO molecules adsorbed perpendicular to the surface. The green and red circles represent Ru atoms in the first (top) and second layers, respectively. The fcc hollow sites are indicated by open red circles. The arrow corresponds to the minimum energy path for H_2 dissociating on the bare Ru surface [26].

the DFT calculations, see Ref. [20] and Chapter 5 of this thesis.

A schematic view of the potential energy surface for H_2 + CO/Ru(0001) [20] is provided by Fig. 6.2 (left panel), which shows a generic view of the potential along the reaction path. As in H_2 + Ru(0001), the minimum overall barrier to dissociation (of 0.29 eV) occurs for H_2 dissociating over the top site (Fig. 6.2, left panel), with the atoms moving in the direction of hcp and fcc three-fold hollow sites (the light blue configuration in Fig. 6.2, right panel). The threefold sites are the preferred atomic chemisorption sites on bare Ru(0001) [25]. Next, the system passes through a molecular chemisorption minimum (the gray configuration in Fig. 6.2, right panel). As the dissociation proceeds, the H atoms increasingly feel the presence of the adsorbed CO molecules. As a result of the presence of the adsorbed CO molecules, the threefold hollow sites are no longer the preferred atomic chemisorption sites; Instead, the H atoms prefer to adsorb to sites close to the hollow sites (these sites are indicated by the orange squares in Fig. 6.2, right panel), but further removed from the CO-molecules than the hollow sites. To reach this dissociated geometry, the center-of-mass of the molecule has to diffuse away from the top site, which gives rise to a second, lower barrier (of 0.23 eV). The complex potential energy landscape illustrated by Fig. 6.2 may be expected to give rise to a complex dynamics, with resonances contributing an oscillatory structure to reaction probabilities computed with quantum dynamics.

Modified Shepard interpolation method

In the modified Shepard (MS) interpolation method, the interpolated PES is given by a weighted series of second order Taylor expansions centered on DFT data points, sampled throughout the configuration space of the system. Instead of the interatomic distances R_i, the inverse interatomic distances, $Q_i = 1/R_i$, are used to describe the PES, which gives a
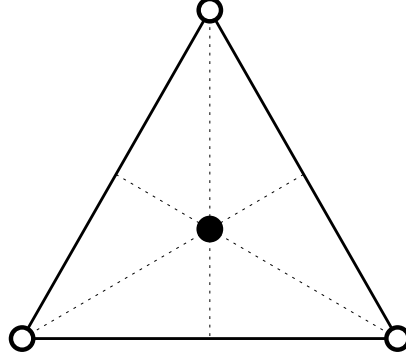
Figure 6.3: Symmetry unique area of the CO/Ru(0001)-($\sqrt{3}$x$\sqrt{3}$)R30° unit cell, where the PES is built by applying the MS interpolation method. The white circles represent CO molecules adsorbed perpendicularly to the surface. The black circles represent the Ru atoms in the first (top) layer (three Ru atoms are below the CO molecules). Four atoms are used to represent the surface in our model: The three O atoms at the corners of the triangle, and the Ru atom at its center. There is a threefold rotational axis passing through the centered Ru atom, and perpendicular to the surface.

better mathematical behavior (the singularities at $R_i \to 0$, when any two atoms are close to each other, are transformed away to $Q_i \to \infty$). The vector defining any configuration of the system is given by $\mathbf{Q} = [1/R_1, ..., 1/R_{n(n-1)/2}]$, where n is the number of atoms used to describe the system. We modeled the CO/Ru(0001) by using the symmetry unique area of the ($\sqrt{3}$x$\sqrt{3}$)R30° surface unit cell, *i.e.* the equilateral triangle in Fig. 6.3, which is half of the ($\sqrt{3}$x$\sqrt{3}$)R30° unit cell. Six atoms were used to describe the H$_2$ + CO/Ru(0001) interaction: The two hydrogen atoms of the H$_2$ molecule approaching the surface, and four surface atoms (three O atoms at the corners of the equilateral triangle, and a Ru atom at the center, see Fig. 6.3). We have also tested other representations of the surface, but they gave either worse results (*e.g.* if the Ru atom at the center of the triangle is not taken into account), or similar results while consuming much more CPU time (*e.g.* if also the three C atoms located below the O atoms are considered).

In our case, $n = 6$, so we have $n(n-1)/2 = 15$ interatomic distances. However, the PES is a function of only $3n - 6 = 12$ independent internal coordinates (eliminating the six translational and rotational degrees of freedom). For each system configuration, the $3n - 6$ internal coordinates, ζ, are defined as linear combinations of the inverse interatomic distances $\mathbf{Q}$ [12]:

$$\zeta_m = \sum_{k=1}^{n(n-1)/2} U_{mk}Q_k \qquad (m = 1, ..., 3n - 6). \qquad (6.1)$$

Note that different configurations $\mathbf{Q}$ of the system will have different transformation matrices $\mathbf{U}$, and therefore different definitions of the (local) internal coordinates ζ [12]. The potential energy at any configuration $\mathbf{Q}$, near data point $\mathbf{Q}(i)$, can be expanded as a second-order Taylor expansion $T_i(\mathbf{Q})$:

$$T_i(\mathbf{Q}) = V[\mathbf{Q}(i)] + \sum_{k=1}^{3n-6} [\zeta_k - \zeta_k(i)] \frac{\partial V}{\partial \zeta_k}\bigg|_{\mathbf{Q}=\mathbf{Q}(i)}$$

$$+ \frac{1}{2} \sum_{k=1}^{3n-6} \sum_{j=1}^{3n-6} [\zeta_k - \zeta_k(i)][\zeta_j - \zeta_j(i)] \frac{\partial^2 V}{\partial \zeta_k \delta \zeta_j}\bigg|_{\mathbf{Q}=\mathbf{Q}(i)} + \ldots \tag{6.2}$$

Here $V[\mathbf{Q}(i)]$, the value of the potential energy at data point $\mathbf{Q}(i)$, and the gradients with respect to ζ at this point were calculated analytically with DFT. The second derivatives of the potential were calculated using numerical forward finite differences of the gradients.

The interpolated potential energy at any configuration Q is then given by

$$V(\mathbf{Q}) = \sum_{g \in G} \sum_{i=1}^{N_{data}} w_{g \circ i}(\mathbf{Q}) T_{g \circ i}(\mathbf{Q}), \tag{6.3}$$

where $T_{g \circ i}(\mathbf{Q})$ represents a second-order Taylor expansion, and $w_{g \circ i}(\mathbf{Q})$ a normalized weight function (for more details see Refs. [12] and [14]). N_{data} is the number of DFT data points in the interpolation, G is the symmetry group of the system and $g \circ i$ is the transformation of the ith data point by the group element g. To take into account the symmetry of the system, a sum is performed over both the DFT data points and all their symmetry equivalent points. In the MS interpolation method the sampling of DFT data points is not uniformly distributed over the configuration space, which presents an advantage over other interpolation methods, which require a regular grid of data points (see *e.g.* Refs. [27] and [28]). In the dynamically important regions of the PES, a larger number of data points is computed. These regions are found by performing classical trajectory calculations. The philosophy behind this method is that it is only necessary to know the PES in that region of space where the dynamics takes place. New points were chosen and added to the PES data set according to one of the following criteria [11–13]: (i) The h-weight criterion, where it is assumed that the new point should be added in the region which is most frequently visited by the classical trajectories, unless (too) many data points are already present there, and (ii) the variance criterion, where it is assumed that a new point should be added in the region where the extrapolation of the Taylor expansion is the most inaccurate.

'Growth' of the PES data set

The PES data set was 'grown' according to the following iterative scheme [11–13]:
(i) We started with an initial PES data set, which contained 105 data points located along six different reaction paths. Those reaction paths were found from DFT results obtained from 2D (r, Z) cuts through the full 6D PES, and by (adaptive) nudged elastic band calculations (see Ref. [20] and Chapter 5 of this thesis for further details).
(ii) Using this initial PES 10 classical trajectories were run on the interpolated PES.
(iii) From the configurations visited by these classical trajectories a new point was chosen and added to the PES data set according to one of the above described criteria.
(iv) After updating the PES data set by adding the new point, the grow process was continued at the second step.

Table 6.1: Kinetic energies and rovibrational states (v, J, m_J) for which the PES data set was 'grown'.

Kinetic energy / eV	v	J	m_J
0.3	0	0	0
0.3	0	3	3
0.3	1	1	0
0.3	1	1	1
0.5	0	0	0
0.5	0	3	0
0.5	0	3	1
0.5	0	3	2
0.5	0	3	3
0.8	0	0	0
0.8	0	3	0
0.8	0	3	3

(v) After ~ 200 new points were added to the PES, its accuracy was checked by computing the reaction and scattering probabilities from a classical trajectory simulation using 5000 trajectories per set of initial conditions. If the reaction probability was not converged (*i.e.* if the reaction probability curve differed from the one computed in the previous simulation based on a smaller potential data base), we returned to the second step and continued the process. Otherwise, when convergence was achieved, the grow process was stopped.

To ensure an accurate representation of the PES over the whole energy range possibly probed by a molecular beam for hydrogen molecules, we grew the PES simultaneously at several kinetic energies and rovibrational quantum states (see Table 6.1). In the grow process we only considered H₂ molecules colliding at normal incidence. To obtain an accurate PES for H₂ + CO/Ru(0001) the grow process had to continue until 3495 extra data points in addition to the 105 initial points were added to the PES data set. The location of the PES data points (both the initial and the added ones) is shown in Fig. 6.4, in (X, Y) and (r, Z) 2D subspaces. We note that Fig. 6.4, left panel, shows the actually calculated data points, as well as their symmetry equivalent ones, obtained by rotating 120° and 240° around the three-fold axis (see Fig. 6.3). Figure 6.5 shows the results of the convergence of the reaction probability for kinetic energies of 0.3 and 0.8 eV, and for a few selected initial states.

6.2.2   Quasi-classical trajectory calculations

To find the dynamically important regions of the PES during the grow process and to calculate reaction probabilities, we performed quasi-classical trajectory (QCT) calculations [29]. The initial zero point energy (ZPE) of the hydrogen molecule was included in the dynamics by using an ensemble of initial conditions for the internal motion of the molecules that forms a classical microcanonical distribution. QCT calculations are susceptible to the so-called ZPE violation problem [30]. However, for an activated process such as H₂ dissociation on CO/Ru(0001), this problem is expected to play only a minor role at energies above the threshold to reaction, and the QCT method is known to give accurate results for activated

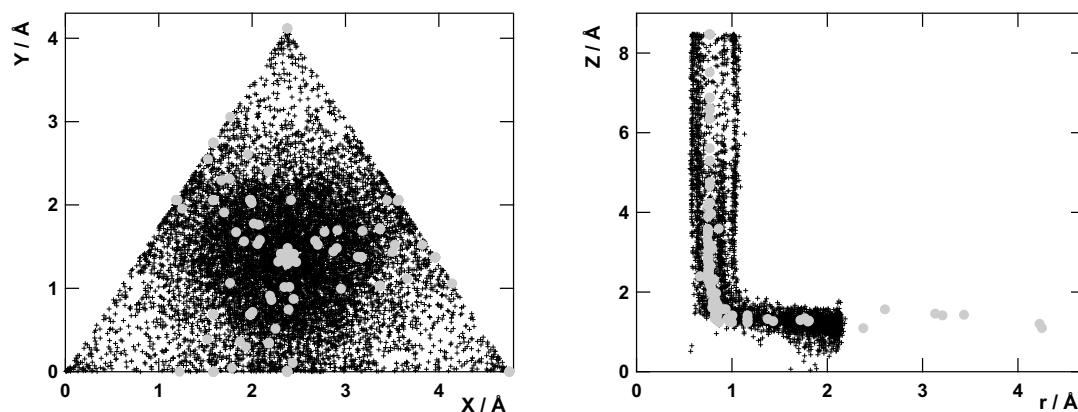**Figure 6.4**: The initial data points of the PES data set (gray) and those added by the grow algorithm (black) shown in (X, Y) representation (left panel) and in (r, Z) representation (right panel).
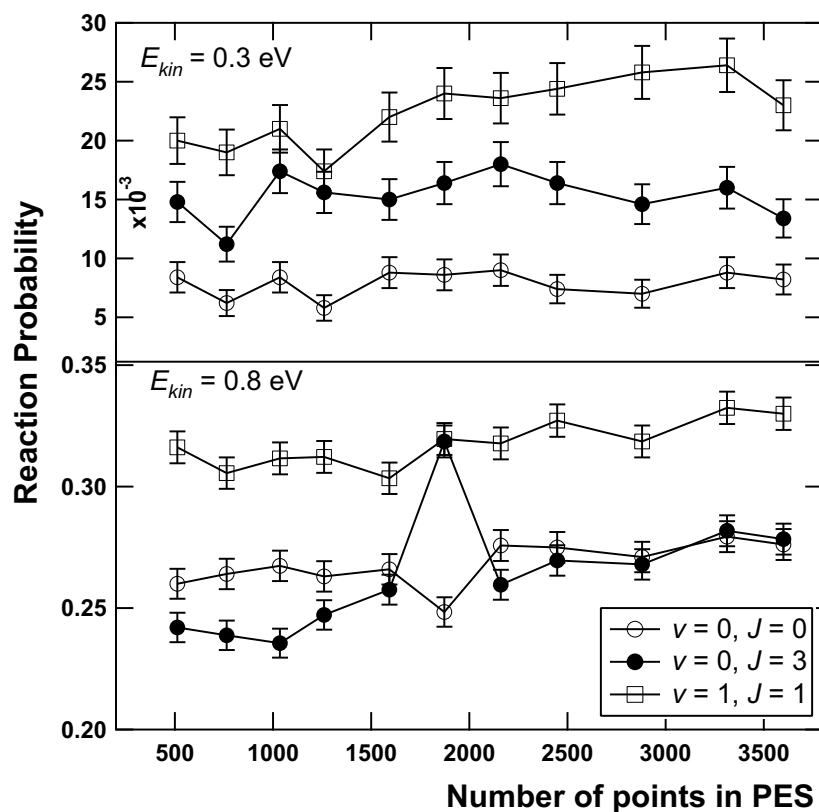

Figure 6.5: Convergence of the H_2 reaction probability with respect to the number of data points in the PES versus the reaction probability for kinetic energies of 0.3 eV (top panel) and 0.8 eV (bottom panel).

molecule-surface reactions [31–37]. In contrast to the fully classical method, vibrational softening (adiabatic transfer of energy from internal to translational motion) is taken into account in an approximate way, whereas not doing this may lead to underestimated reaction probabilities for activated dissociation [34]. As noted below, we perform a quantum dynamics calculation for one initial rovibrational state to validate the use of the quasi-classical trajectory method [36].

To compute the reaction probability of hydrogen we integrated the classical equations of motion using the velocity-Verlet algorithm [38]. For each initial kinetic energy (E_{kin}) and initial rovibrational state (v, J, m_J), the probabilities have been calculated as an average over the molecular initial conditions, *i.e.* internal coordinates and internal momenta conjugate to these coordinates. To obtain the molecular initial conditions for each set of initial parameters E_{kin}, v, J and m_J, a Monte Carlo sampling method has been used. In order to minimize the statistical errors we have computed 5000 trajectories for each value of E_{kin} and rovibrational state (v, J, m_J) of H$_2$ (D$_2$). This leads to a maximum error in the reaction probabilities reported of 0.007. We have used an integration time step of 0.01 a.u. (*i.e.* 2.4×10^{-4} fs) and a total propagation time of 5000 a.u (*i.e.* 121 fs). The allowed error in the energy conservation of each trajectory has been set to 10^{-3} a.u. (*i.e.* 27 meV). We consider that dissociation has taken place whenever $r > 4a_0$ (2.1 Å) with a positive radial velocity of H$_2$. In contrast, a molecule is considered reflected when the molecular center-of-mass Z reached its starting point with the molecule's velocity vector pointing towards the vacuum.

To compute reaction probabilities as a function of m_J the initial angular momentum of the molecule was fixed according to $|\mathbf{L}| = \sqrt{J(J+1)}$. The orientation of $\mathbf{L}$ was chosen randomly with the constraint:

$$cos(\theta_L) = \frac{m_J}{\sqrt{J(J+1)}}, \tag{6.4}$$

where θ_L is the angle between $\mathbf{L}$ and the Z-axis (the axis perpendicular to the surface).

6.2.3   Quantum dynamics calculations

Quantum dynamics calculations were performed by solving the time-dependent Schrödinger equation using the time-dependent wave packet (TDWP) method [39] in an implementation described in Ref. [34].

The initial state of the system $[\Psi(t=0; \mathbf{r}, \mathbf{R})$, where $\mathbf{r} = (r, \theta, \varphi$ and $\mathbf{R} = (X, Y, Z)]$ is represented by the product of a Gaussian wave packet in Z and the rovibrational eigenfunctions of H$_2$ (v, J, m_J). For normal incidence

$$\Psi(t=0; \mathbf{r}, \mathbf{R}) = N\varphi_{vJ}(r)Y_{Jm_J}(\theta, \varphi)e^{-\alpha(Z-Z_0)^2 + ik_{av}Z}, \tag{6.5}$$

where the vibrational eigenfunction $\varphi_{vJ}(r)$ and the spherical harmonic $Y_{Jm_J}(\theta, \varphi)$ together describe the initial rovibrational state of the hydrogen molecule, N is a factor normalizing the wave packet, α is the width of the wave packet in Z and k_{av} is the average translational momentum of H$_2$ towards the surface.

To represent the dependence of the wave function on Z, r, X and Y, a direct product discrete variable representation (DVR) [40] with constant grid spacings $\Delta Z, \Delta r, \Delta X$ and

ΔY is used. Fast Fourier transforms [41, 42] are used to transform the wave function from coordinate to momentum space, and vice versa. To represent the dependence of the wave function on θ and φ, a non-direct product finite basis representation (FBR) of spherical harmonics $Y_{Jm_J}(\theta, \varphi)$ is used. Gauss-Legendre and Fourier transformations are used to transform the wave function from the non-direct product FBR to a direct product DVR in θ and φ [43, 44], respectively, and vice versa.

To propagate the wave packet in time the split operator method [41] is used. The part of the wave packet that is reflected from the surface is analyzed [45], integrated over time and the S-matrix elements for all open rotation, vibration and diffraction channels are obtained. State-to-state scattering probabilities are computed from the S-matrix elements. All these scattering probabilities are summed over final states and subtracted from unity to obtain the initial-state-selected reaction probability. For more details we refer the reader to Refs. [36, 46].

The parameters used in the calculations are described below. The values are given in Table 6.2 for the two different wave packets used, one for low kinetic energy (0.1-0.35 eV) and one for high kinetic energy (0.3-0.8 eV). The initial wave packet was defined by the initial position of the center of the wave packet (Z_0) and its average initial momentum (k_{av}). The calculation is done on the Z grid, which is defined by its minimum value in Z, Z_i, the spacing ΔZ, and the number of grid points N_Z. To speed up the calculation, a projection operator approach [47] is used, in which the initial wave packet is moved towards the surface on a two-dimensional grid in Z and r, that is longer in Z than the 6D grid. This 2D grid is called the specular grid, and its number of points in the Z direction is given by N_Z^{sp}. The grid in r is defined in the same way as the grid in Z. The grid in X and Y is a periodic grid with a periodicity defined by the lattice constant and the number of grid points N_X and N_Y. The basis set in θ and φ is given by the maximum J value, J_{max}.

The reflected wave packet was analyzed at Z_∞, which is far enough from the surface to ensure that there is no interaction between the molecule and the surface. The wave packet is propagated in time with a time step Δt. We added an optical potential [48] to the Z and r grid to absorb the reflected (reacted) part of the wave packet before it reached the end of the grid. The optical potential is characterized by its start value, the range over which it extends and the value for the translational energy (here called the optical energy) for which the optimum absorption takes place [48].

6.2.4   Molecular beam simulation

In a supersonic molecular beam experiment, the temperature of the expansion nozzle, T_n, determines the average kinetic energy (E_n ranging from 2.5 to $2.7RT_n$), the vibrational temperature ($T_{vib} = T_n$) and the rotational temperature ($T_{rot} = 0.8T_n$) [49] of the impinging hydrogen molecules. To compare our computed reaction probabilities to experimental results obtained for the same system [10], we have made a simulation of the molecular beam conditions used in the experiment, taking into account the collision energy (velocity) distribution of the beam, and the vibrational and rotational states populated at the different nozzle temperatures. The computed total reaction probability $R(T_n)$, which will be compared to the measured reaction probability $S_0(T_n)$ (we use R for computed and S_0 for measured values), can be calculated from the energy-resolved reaction probabilities $R(E_n; T_n)$ convoluted with the velocity distribution of the supersonic molecular beam by:

Table 6.2: Parameters used in the TDWP calculations. All values are in atomic units, unless stated otherwise. See <u>text for details.</u>

	Energy range (eV)	
Parameter	0.1-0.35	0.3-0.8
Initial wave packet		
Initial position Z_0	18.5	18.0
Average initial momentum k_{av}	7.46	12.21
Grid parameters		
Z_i	1.49	1.49
N_Z	128	128
N_Z^{sp}	256	256
Grid spacing ΔZ	0.15	0.15
r_i	0.4	0.4
N_r	32	32
Grid spacing Δr	0.25	0.25
N_X (N_Y)	32	48
Lattice constant	8.98	8.98
J_{max} rotational basis	18	18
Time propagation		
Time step Δt	2.5	2.5
Propagation time	120000	60000
Z optical potential		
Start optical potential	15.9	16.4
Optical energy	3.7×10^{-4}	3.7×10^{-4}
Range	3.15	3.65
r optical potential		
Start optical potential	4.15	4.15
Optical energy	3.7×10^{-3}	3.7×10^{-3}
Range	4.0	4.0
Other parameters		
Analysis value Z_∞	15.7	15.7

$$R(T_n) = \frac{\int_0^\infty f(v; T_n) R(E_n; T_n) dv}{\int_0^\infty f(v; T_n) dv}. \tag{6.6}$$

Here the flux weighted velocity distribution for a nozzle temperature T_n is given by [50,51]:

$$f(v; T_n) = C v^3 e^{\frac{-(v-v_0)^2}{\alpha^2}}, \tag{6.7}$$

where C is a constant, v is the velocity, v_0 is the stream velocity and α is the width of the velocity distribution. Note that the parameters C, v_0 and α depend on the nozzle temperature.

In Eq. 6.6 $R(E_n; T_n)$ is the energy-resolved reaction probability given by:

$$R(E_n; T_n) = \sum_{v,J} F_B(v, J, T_n) R(E_n; v, J). \tag{6.8}$$

Here $R(E_n; v, J)$ is the energy resolved initial-state-selected reaction probability and the Boltzmann factor F_B is given by:

$$F_B(v, J, T_n) = e^{-E_{vib}(v)/kT_n} (2J+1) e^{-E_{rot}^v(J)/0.8kT_n} / N, \tag{6.9}$$

where N is a normalization factor:

$$N = \sum_{v,J} e^{-E_{vib}(v)/kT_n} (2J+1) e^{-E_{rot}^v(J)/0.8kT_n}, \tag{6.10}$$

and the vibrational and rotational energies are taken as [52]:

$$E_{vib}(v) = \left(v + \frac{1}{2}\right)\omega_e - \left(v + \frac{1}{2}\right)^2 \omega_e x_e + \left(v + \frac{1}{2}\right)^3 \omega_e y_e \tag{6.11}$$

$$E_{rot}^v(J) = B_e J(J+1) - \alpha_e \left(v + \frac{1}{2}\right) J(J+1). \tag{6.12}$$

The constants ω_e, $\omega_e x_e$, $\omega_e y_e$, B_e and α_e were taken from Ref. [52]. For the calculation of the rotational and vibrational fractions $F_B(v, J, m_J)$ used, the presence of ortho and para hydrogen in the molecular beam was taken into account (ortho= 75% for H_2 and 67% for D_2, and para= 25% for H_2 and 33% for D_2) by multiplying the obtained fraction $F_B(v, J, m_J)$ with the appropriate fraction of ortho or para hydrogen.

To obtain the total computed reaction probability, we have carried out QCT calculations for a selection of relevant kinetic energies, and all relevant vibrational and rotational states. The 10-12 kinetic energy data points obtained for all rovibrational states were interpolated using a cubic spline method. The energy distribution of the molecular beam was numerically integrated using points with equal spacing in the energy, and for each of these energies the reaction probability was taken from the cubic spline fit interpolation.
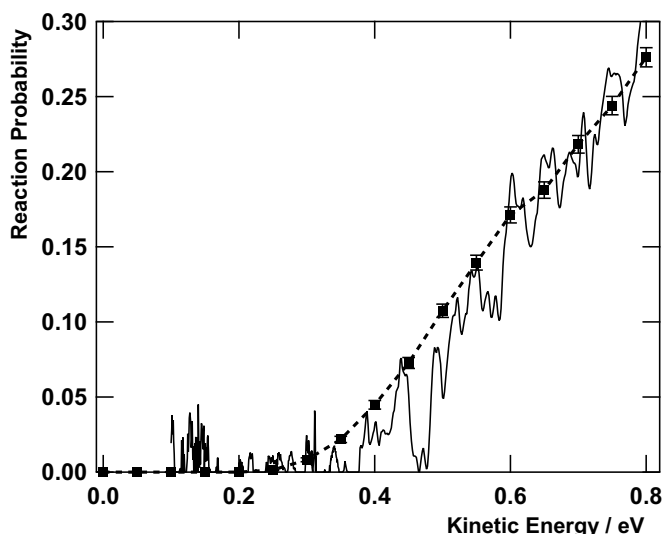
Figure 6.6: Comparison of quantum and quasi-classical reaction probabilities for the rovibrational ground state of H_2 ($v = J = m_J = 0$). Solid line: quantum dynamics results. Filled squares with error bars: QCT results (The dashed line is to guide the eye).

6.3   Results and discussion

Using the described methods we have calculated the reaction probability of hydrogen on CO/Ru(0001). First we compare the results obtained with quantum dynamics (QD) calculations with those obtained with quasi-classical trajectory (QCT) calculations for H_2. Figure 6.6 shows this comparison for the rovibrational ground state. The oscillations in the QD results are caused by resonances. Because we compute the quantum reaction probabilities as one minus the sum of the scattering probabilities [34, 46], an artifact of the calculations being not completely converged with respect to propagation time, is that near resonance features negative reaction probabilities may be obtained with this procedure. In this case, we simply set them to zero. Both QCT and the main envelop of the QD results show a reaction probability that is zero at low kinetic energy and increases with increasing kinetic energy. This behavior is characteristic of activated adsorption and was also found experimentally for CO-precovered Ru(0001) [10]. The activated adsorption was also found in a theoretical study of the bare Ru surface [2]. The fact that up to ∼0.3 eV no reaction is seen from the reaction probability of Fig. 6.6 compares well to the lowest barrier found for this system (0.29 eV) [20]. In general, the agreement between quantum dynamics and quasi-classical trajectory results is good, justifying that all other results presented in this paper are obtained by quasi-classical trajectory calculations, which are computationally much cheaper. At the lower collision energies the QCT reaction probabilities are somewhat higher than the QD results, presumably because the molecule converts too much of its ZPE to energy in motion along the reaction path in the QC dynamics.

To study the influence of rotational states on the reaction probability we obtained results for H_2 with $v = 0$, $J = 0 - 7$, and D_2 with $v = 0$, $J = 0 - 11$, and averaged over m_J:
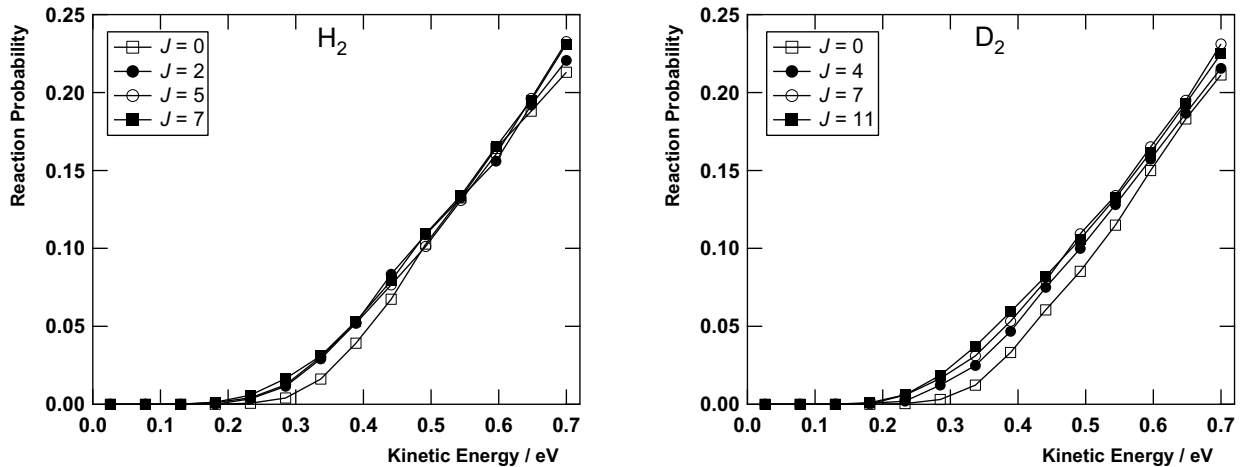
Figure 6.7: Reaction probabilities computed with the QCT method are shown as a function of J for several $(v = 0, J)$ states of H_2 and D_2.

$$R_J(E) = \frac{1}{2J+1} \sum_{m_J=-J}^{J} R_{J,m_J}(E). \tag{6.13}$$

The rotational states we have calculated are those significantly ($\geq 1\%$) populated in the supersonic molecular beam at the different nozzle temperatures used in the experiment. Figure 6.7 shows a selection of these results. We find that for all J rotational states the adsorption is direct and activated, as found for the rovibrational ground state as well. The rovibrational ground state has the lowest reactivity, both for H_2 and D_2. For $J = 1$ the reaction probability increases slightly (not shown). For the H_2 rotational states with $J = $ 2-7 no significant difference is seen, but they all show higher reactivity than the ground state, indicating that rotational excitation enhances reaction. This is in agreement with calculations for H_2 dissociation on Cu(100) where it was found that the reaction probability of $J = 4$ is higher than that of $J = 0$ [31]. On the other hand, for Pd(100) the calculated reaction probability decreases when increasing the rotational quantum number J from 0 to 4 [53]. Experiments on Cu(111) [54] also observed rotational hindering for $J \leq 4$, as was found in a theoretical study of the same surface [55]. However, these authors observed the inverse trend (higher J shows higher reactivity) for $J > 4$. For D_2 we also observe that rotational excitation enhances reactivity.

For comparison we have investigated the same rotational states as shown in Fig. 6.7, but now for $m_J = 0$. Figure 6.8 shows the same selection of these results as is shown for the orientationally averaged rotational states. We observe that for high rotational states ($J > 4$, some not shown) the reaction probability becomes lower with higher rotational quantum number J. This indicates that for molecules that are rotating faster it is more difficult to be steered into orientations favorable for reaction. For $J < 4$ (some not shown) the results lie closer together. For kinetic energies below 0.5 eV, $J = 2, 3$ show higher reactivity than the rovibrational ground state. For $J = 1$ the results are very similar to $J = 0$.

Figure 6.9 shows a comparison between some rotational states with $m_J = 0$ (cartwheel
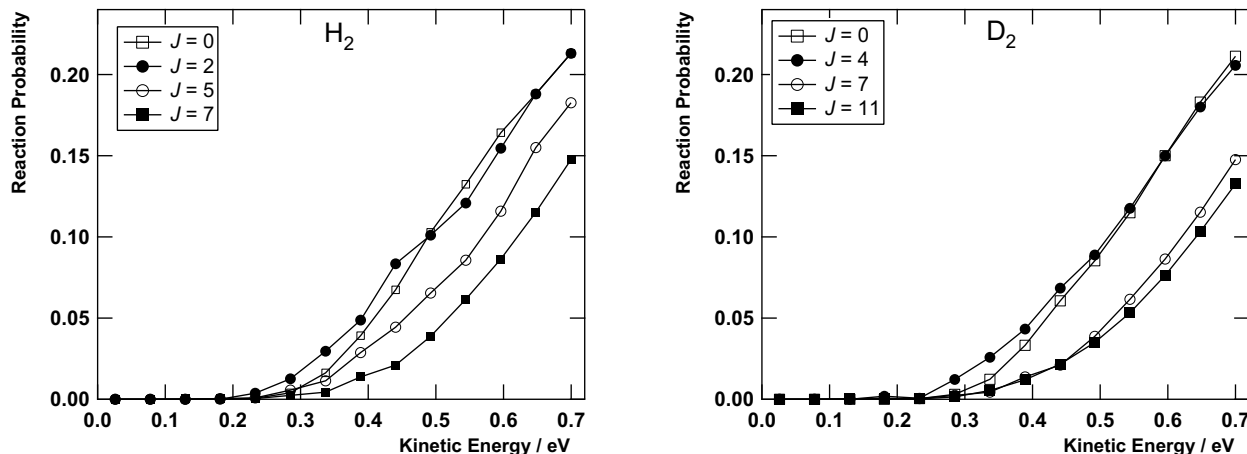
Figure 6.8: QCT results for the vibrational ground state ($v = 0$) of H$_2$ (left panel) and D$_2$ (right panel) where J is varied and $m_J = 0$.

molecules) and $m_J = J$ (helicopter molecules). From Fig. 6.9 it is clear that helicopter molecules have significantly higher reactivity than the corresponding cartwheel molecules. This is even clearer from Fig. 6.10, where a plot is shown of reaction probability versus rotational quantum number J for the cartwheel and helicopter orientations, and for the orientationally averaged results, for both H$_2$ and D$_2$, and kinetic energies of 0.34 and 0.70 eV. Especially for high J, molecules in the helicopter orientation have the highest reaction probability, followed by the orientationally averaged states, and the cartwheel molecules show the lowest reactivity. The fact that helicopter states show higher reaction probability is also observed for Pd(100) [53,56,57], Cu(100) [58] and Cu(111) [59,60]. It can be explained by the fact that the helicopter state samples more orientations of the molecule parallel to the surface, which is favorable to reaction. The effect is similar for H$_2$ and D$_2$, and more pronounced at low kinetic energy (enhancement of factor ~ 10) than at high kinetic energy (enhancement of factor $\sim 2 - 3$), and more for high J than for low J.

In addition to the influence of excited rotational states on the reaction probability, we also investigated the influence of excitation to the first vibrational level. Figure 6.11 shows a comparison between $v = 0$ and $v = 1$ for the rotational ground state. From this figure it is clear that significant vibrational enhancement exists. At first, this might seem contradictory with the fact that the barrier is located in the entrance channel (early barrier system), where the reduced mass associated with the vibration perpendicular to the reaction path changes only very little as the molecule approaches the barrier. However, it is possible that the force constant associated with the vibration decreases towards the barrier. As a consequence, the vibrational energy becomes smaller as the molecule approaches the barrier, even though there is little or no change in the reduced mass associated with the vibration perpendicular to the reaction path. For $v = 1$ H$_2$, even more vibrational energy is released, resulting in the observed vibrational enhancement. The same behavior has been observed for both early barrier systems such as H$_2$ + Pt(111) [46,61], and for non-activated systems such as H$_2$ + Pd(100) [62].

To compare theoretical results obtained in this study to experimental data for the same
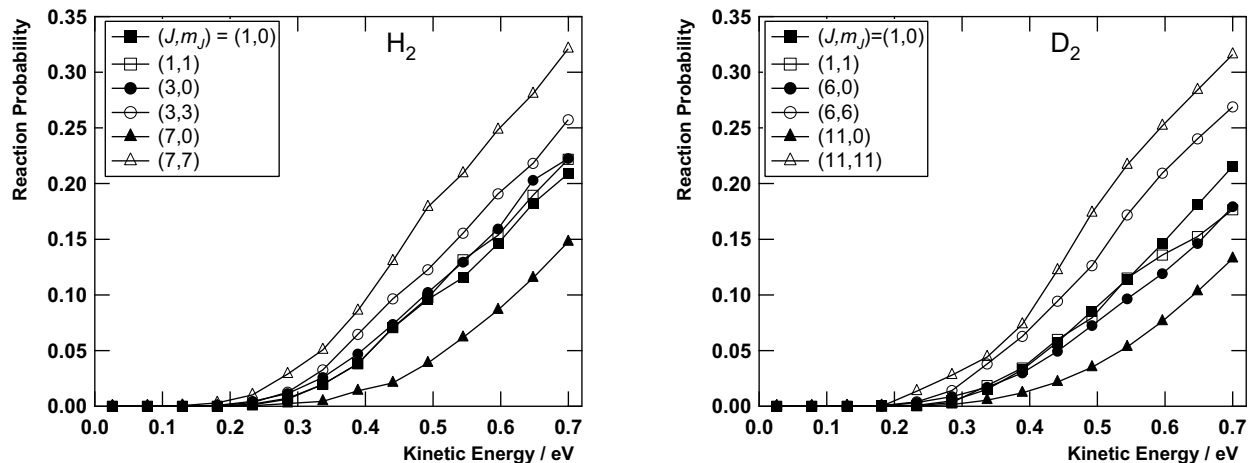
Figure 6.9: QCT results for the vibrational ground state ($v = 0$) of H_2 (left panel) and D_2 (right panel) where J is varied and $m_J = 0$ or $m_J = J$.

system [10], we have first investigated the influence of the collision energy distribution of the supersonic molecular beam on the reaction probability, as well as the influence of rovibrational states that are populated. First, we have convoluted the rovibrational ground state reaction probability obtained from QCT calculations with the energy distribution of the supersonic molecular beam used in the experiments (for the parameters that describe the energy distribution corresponding to the velocity distribution of Eqs. 6.6 and 6.7 see Table 6.3). The results are shown in Fig. 6.12 for both H_2 and D_2. At higher kinetic energy (above 0.3 eV) a small isotope effect is observed: H_2 shows higher reactivity than D_2 (see Fig. 6.12 top panel). When convoluting the rovibrational ground state with the energy distribution of the supersonic molecular beam, we observe that the reactivity increases. This is due to the fact that the energy distribution is not symmetric: At the high kinetic energy side the tail is longer than at the low kinetic energy side (see Fig. 6.13). Since the system shows direct, activated behavior (*i.e.* increasing reaction probability with increasing kinetic energy), the molecules present in the high kinetic energy part of the distribution contribute to a higher reaction probability. The difference between the rovibrational ground state and the energy convoluted data is most pronounced at high kinetic energy. This is due to the fact that the energy distribution of the supersonic molecular beam becomes broader at higher kinetic energy. The higher the nozzle temperature, the broader the energy distribution is. The effect of increasing the nozzle temperature on the energy distribution is shown in Ref. [1]. If for a given nozzle temperature, the ratio between carrier gas (here: H_2) and seeded gas (here: D_2) is lower, the energy distribution becomes broader as well (see Fig. 6.13). The two highest kinetic energy data in Fig. 6.12 were obtained experimentally by seeding D_2 in H_2 in a 1:1 and 1:2 ratio, respectively (the presence of H_2 accelerates the D_2 molecules and hence their kinetic energy increases). In Fig. 6.12, we show the kinetic energy range that was used in the experiments. For a detailed overview of the energy distribution of the experiments see Ref. [1].

To investigate the influence of the population of the rotational and vibrational states in the molecular beam on the measured reaction probability we calculated the percentages of
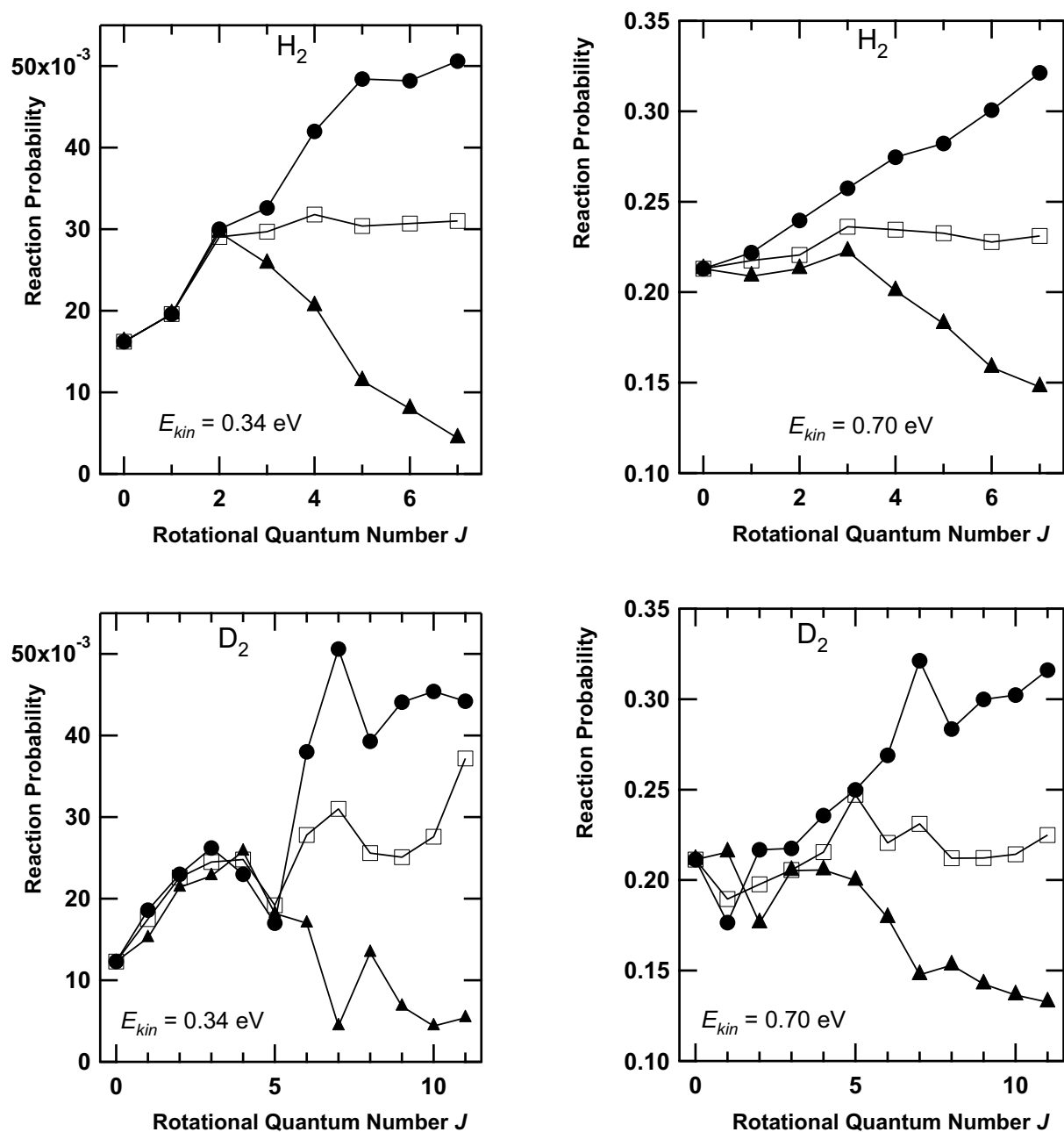
Figure 6.10: Reaction probability versus initial rotational quantum number J for H_2 (top panels) and D_2 (bottom panels) for $E_{kin} = 0.34$ eV (left panels) and $E_{kin} = 0.70$ eV (right panels). Open squares: m_J- averaged reaction probability [Eq. 6.13]; filled circles: $m_J = J$ (helicopter orientations); filled triangles: $m_J = 0$ (cartwheel orientations).
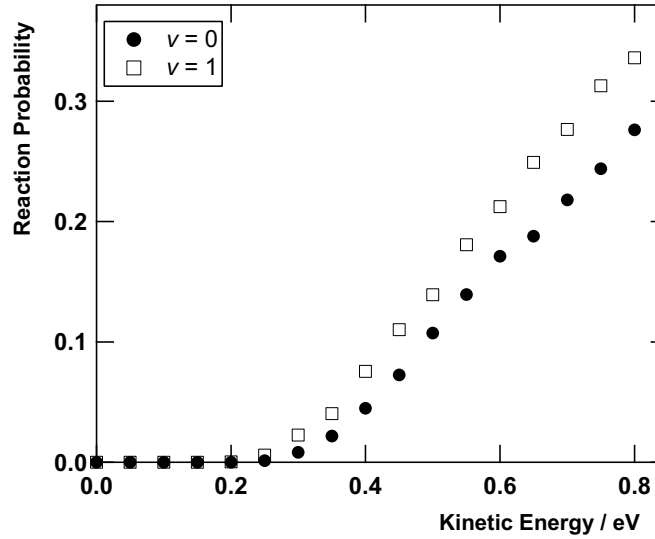
Figure 6.11: Comparison between the reactivity of the vibrational ground state ($v = 0$) and first excited state ($v = 1$) for $J = 0$.

Table 6.3: Fit parameters for the experimental velocity distributions of the incident molecular beam. The density weighted velocity distribution of the incident molecular beam which was measured using time-of-flight and mass spectrometry [1], is fitted with the following formula: $f(v) = C * v^2 * exp\left(-\frac{(v-v_0)^2}{\alpha^2} \right)$. Here C is a constant, v is the velocity in m s^{-1}, and α is the width of the distribution in m s^{-1}. The kinetic energy given is taken from the peak of the density weighted energy distribution (most probable energy).

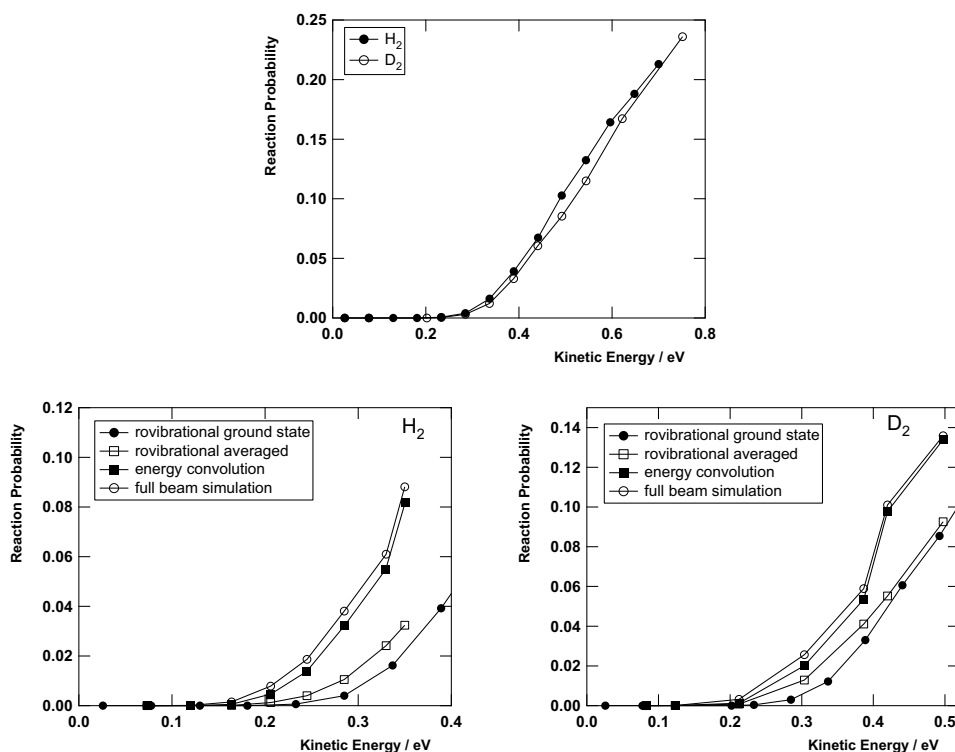| Isotope	Seed ratio (xH$_2$:yD$_2$)	T_n / K	E_{kin} / eV	v_0 / m s^{-1}	α / m s^{-1}
H$_2$		300	0.073	2662	314.1
		500	0.12	3388	575.2
		700	0.16	3956	795.5
		900	0.21	4404	1007
		1100	0.24	4741	1165
		1300	0.29	5132	1346
		1500	0.33	5436	1528
		1700	0.35	5737	1705
D$_2$		300	0.083	1942	193.5
		500	0.12	2391	291.3
		900	0.21	3138	514.3
		1300	0.30	3710	741.3
		1700	0.39	4163	854.3
	1:1	1700	0.42	4367	1179
	2:1	1700	0.50	4834	1065

Figure 6.12: Top panel: Comparison between the rovibrational ground state reaction probability of H_2 and D_2. Bottom panels: Comparison between the quasi-classical reaction probability for the rovibrational ground state, and such probabilities averaged over rovibrational states and/or convolved with the energy distributions of the supersonic molecular beam used in the experiment [10]. Left panel: H_2; right panel: D_2.
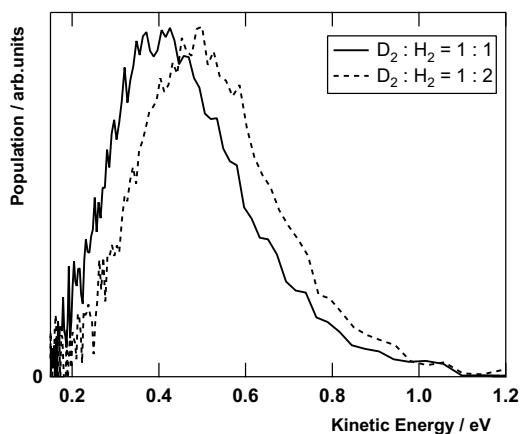

Figure 6.13: The collision energy distribution of D_2 in the molecular beam used in the experiments [1,10] shown for nozzle temperatures of $T_n =$ 1700 K, for beams of D_2 seeded in H_2.

all states populated in the supersonic molecular beam under the experimental conditions and their contribution to the reaction probability, as explained in Sec. 6.2.4. For both H_2 and D_2 we took into account the $v = 0$ and $v = 1$ states. For H_2 rotational states up to $J = 9$ were taken into account, and for D_2, where the rotational levels are more closely spaced, we took into account levels up to $J = 15$. The results of averaging the reaction probability over the rovibrational states populated in the molecular beam is also shown in Fig. 6.12. We observe that the reactivity increases with respect to the rovibrational ground state reaction probability. When comparing the effect of the energy distribution and the rovibrational states population, we observe that taking into account the collision energy distribution has a much larger effect on the reactivity than averaging over all rovibrational states populated in the beam.

The results of the total supersonic molecular beam simulation (collision energy distribution and rovibrational states) are also shown in Fig. 6.12 for both H_2 and D_2. For comparison also the rovibrational ground state result, the result averaged over the rovibrational states, and the energy convolved result are shown. We observe that the overall shape is similar: The reactivity increases with kinetic energy, indicating that the dissociative adsorption is activated. Below 0.3 eV the reaction probability is zero, again indicative of activated adsorption. The results of the supersonic molecular beam simulation are higher than those of the rovibrational ground state, indicating that the effects of the energy distribution of the molecular beam and the population of excited rotational and vibrational states are to increase the reactivity.

When comparing theoretical and experimental results for D_2 (see Fig. 6.14), we observe a similar trend: Direct adsorption over a distribution of barriers, as was seen as well for the bare Ru(0001) surface [1,2]. However, it is clear that the calculated reactivity is much lower than the measured reaction probability. The calculations show a high barrier to reaction of 0.29 eV [20]. In the experiment an indication is given for non-activated (barrierless) reaction, as was also observed for the bare Ru(0001) surface [1]. When extrapolating the measured reaction probability to zero kinetic energy, a reactivity of ~ 0.05 is observed, indicative of non-activated adsorption.

When calculating the difference in kinetic energy between theory and experiment for which the same reaction probability is observed (see Fig. 6.14), we find $\Delta E = -0.31$ eV for a reaction probability of 0.071, and $\Delta E = -0.23$ eV for a reaction probability of 0.12 (the minus sign indicates that the theoretical kinetic energy is higher for the same reaction probability). This ΔE value can be interpreted as reflecting the mean absolute error of the RPBE functional for reaction barrier heights. For a data base of six H-abstraction gas phase reactions, the mean absolute error in the reaction barrier height was found to be 0.28 eV for the RPBE functional [63]. On the other hand, comparing the difference between theory and experiment in the kinetic energy for which the same reaction probability is observed to the results obtained for bare Ru(0001), we find that in this case the energy differences are much smaller, varying between 3.7×10^{-4} eV and -0.11 eV.

The discrepancy between theory and experiment cannot be due to the energy distribution, since it has been taken into account. It was already suggested before that the energy distribution of the supersonic molecular beam is not the reason for the discrepancy between theoretical and experimental results for H_2 + Ru(0001), for which a very rough convolution was done [1]. The second possible origin of the discrepancy, the population of rovibrational states, is also shown not to be the reason for the observed difference, since in this study
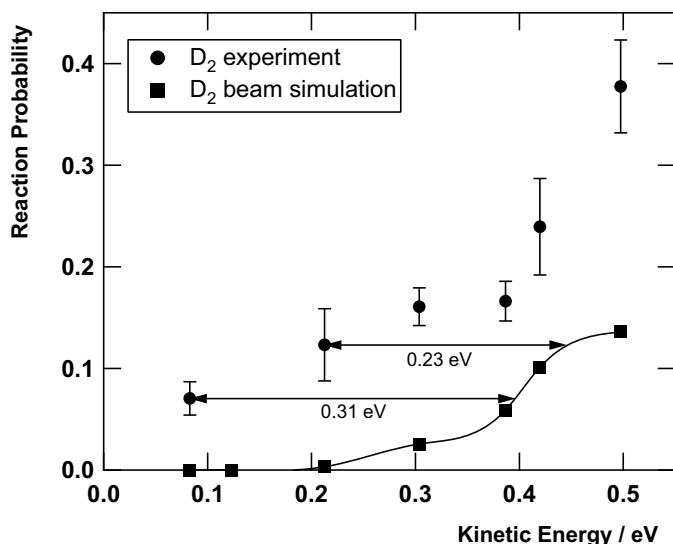
Figure 6.14: Comparison between the reaction probability obtained from the molecular beam simulation (see text for details) and the experimental probability [10] for D$_2$.

they have been taken into account. In fact, our paper shows that for the molecular beam used in this study the effect of rovibrational state averaging is much smaller than that of convoluting with the energy distributions. A third possible origin of the discrepancy lies in the DFT calculations. The RPBE functional was found to overestimate the barrier to H$_2$ dissociation on bare Ru(0001) [1]. This is also observed in the present comparison for H$_2$ + CO/Ru(0001): Theory shows a barrier of 0.29 eV, while experiment suggests barrierless dissociation in addition to an activated mechanism. For the present system, the RPBE functional underestimates reactivity over the whole kinetic energy range compared. The PW91 functional [3], on the other hand, overestimates chemisorption energies, resulting in too high reactivity [1]. At the moment, no indication is available that other standard GGA functionals perform better for these activated systems. However, for bare Ru(0001) the discrepancy between experiment and theoretical predictions using the RPBE functional is much smaller (mean error of 0.31 eV for the CO-precovered surface versus 0.11 eV for the bare surface, see the above explanation). A fourth possible reason for the discrepancy involves the existence of phonons (including the motion of CO relative to the surface) and electron-hole pair excitations in the experiment, which are ignored in the calculations. The incoming hydrogen molecule could cause the CO to move, an aspect that may not be influenced much by surface temperature, and thus could not be ruled out from the experiments. In addition, the fact that the discrepancy between theory and experiment is much smaller for the bare Ru(0001) surface than for CO/Ru(0001) also suggests that the inclusion of the degrees of freedom of CO is necessary. With respect to e-h pair excitations, however, a combined theoretical and experimental study on Pt(111) [6] found that it is justified to ignore these excitations.

6.4   Conclusions

We have built a 6D PES for H_2 + CO/Ru(0001) based on DFT calculations, to perform dynamics simulations of H_2 and D_2 on a CO-precovered Ru surface, using both quantum and quasi-classical dynamics. We find that quantum and classical reaction probabilities for the rovibrational ground state compare well, which justified the use of the QCT method to compute molecular beam simulated reaction probabilities. The reactivity of several excited rotational states has been calculated and compared to that of the rovibrational ground state. It is found that rotation slightly enhances reaction, and that reaction is favored by helicopter orientations of the molecules, as compared to cartwheel orientations. In addition, the population of the first excited vibrational state is found to significantly increase reactivity.

We have compared our theoretical results to the experimental ones, by simulating the experimental supersonic molecular beam, *i.e.* we have taken into account the collision energy distribution and the rovibrational states population characteristic of the experimental molecular beam. We find that the effects of the energy distribution of the molecular beam and the population of excited rovibrational states in the beam are to increase the reactivity compared to that of the rovibrational ground state. The effect of the energy distribution of the supersonic molecular beam is found to be much larger than the effect of the rotational states population. However, even when taking into account these two effects, a significant discrepancy persists between theory and experiment. Both show direct adsorption, but the experimental reaction probability is significantly higher. The calculations find a lowest barrier to dissociation of 0.29 eV, whereas in the experiments an indication of non-activated reaction at low kinetic energies is observed. We argue that these discrepancies could be caused by the neglect of phonons in the theory (including motion of CO to make place for the impinging hydrogen molecule) and/or inaccuracies of the GGA functional used in the DFT calculations.

Acknowledgments

References

[1] I. M. N. Groot, H. Ueta, M. J. T. C. van der Niet, A. W. Kleyn, and L. B. F. Juurlink, J. Chem. Phys. **127**, 244701 (2007).

[2] J. K. Vincent, R. A. Olsen, G. J. Kroes, M. Luppi, and E. J. Baerends, J. Chem. Phys. **122**, 044701 (2005).

[3] P. Ziesche and H. Eschnig, editors, *Electronic structure of solids '91* (Akademie Verlag, Berlin, 1991).

[4] J. P. Perdew, J. A. Chevary, S. H. Vosko, K. A. Jackson, M. R. Pederson, D. J. Singh, and C. Fiolhais, Phys. Rev. B. **46**, 6671 (1992).

[5] B. Hammer, L. B. Hansen, and J. K. Nørskov, Phys. Rev. B. **59**, 7413 (1999).

[6] P. Nieto, E. Pijper, D. Barredo, G. Laurent, R. A. Olsen, E. J. Baerends, G. J. Kroes, and D. Farías, Science **312**, 86 (2006).

[7] J. Gallagher and J. B. Fenn, J. Chem. Phys. **60**, 3492 (1974).

[8] J. E. Pollard, D. J. Trevor, Y. T. Lee, and D. A. Shirley, J. Chem. Phys. **77**, 4818 (1982).

[9] K. Kern, R. David, and G. Comsa, J. Chem. Phys. **82**, 5673 (1985).

[10] H. Ueta, I. M. N. Groot, M. A. Gleeson, S. Stolte, G. C. McBane, L. B. F. Juurlink, and A. W. Kleyn, Chem. Phys. Chem. **9**, 2372 (2008).

[11] M. J. T. Jordan, K. C. Thompson, and M. A. Collins, J. Chem. Phys. **102**, 5647 (1995).

[12] K. C. Thompson, M. J. T. Jordan, and M. A. Collins, J. Chem. Phys. **108**, 8302 (1998).

[13] R. P. A. Bettens and M. A. Collins, J. Chem. Phys. **111**, 816 (1999).

[14] C. Crespos, M. A. Collins, E. Pijper, and G. J. Kroes, J. Chem. Phys. **120**, 2392 (2004).

[15] M. Born and R. Oppenheimer, Ann. Phys. (Leipzig) **389**, 457 (1927).

[16] E. D. Williams and W. Weinberg, Surf. Sci. **82**, 93 (1979).

[17] H. Pfnür, D. Menzel, F. M. Hoffmann, A. Ortega, and A. M. Bradshaw, Surf. Sci. **93**, 431 (1980).

[18] G. Michalk, W. Moritz, H. Pfnür, and D. Menzel, Surf. Sci. **129**, 92 (1983).

[19] H. Pfnür and D. Menzel, Surf. Sci. **148**, 411 (1984).

[20] I. M. N. Groot, J. C. Juanes-Marcos, R. A. Olsen, and G. J. Kroes, J. Chem. Phys. (submitted).

[21] P. Hohenberg and W. Kohn, Phys. Rev. B. **136**, B864 (1964).

[22] W. Kohn and L. J. Sham, Phys. Rev. A. **140**, 1133 (1965).

[23] DACAPO, http://www.camp.dtu.dk/campos/Dacapo/.

[24] E. Christoffersen, P. Stoltze, and J. K. Nørskov, Surf. Sci. **505**, 200 (2002).

[25] M. Lindroos, H. Pfnür, P. Feulner, and D. Menzel, Surf. Sci. **180**, 237 (1987).

[26] M. Luppi, R. A. Olsen, and E. J. Baerends, Phys. Chem. Chem. Phys. **8**, 688 (2006).

[27] H. F. Busnengo, A. Salin, and W. Dong, J. Chem. Phys. **112**, 7641 (2000).

[28] R. A. Olsen, H. F. Busnengo, A. Salin, M. F. Somers, G. J. Kroes, and E. J. Baerends, J. Chem. Phys. **116**, 3841 (2002).

[29] M. Karplus, R. N. Porter, and R. D. Sharma, J. Chem. Phys. **43**, 3259 (1965).

[30] Y. Guo, D. L. Thompson, and T. D. Sewell, J. Chem. Phys. **104**, 576 (1996).

[31] D. A. McCormack and G. J. Kroes, Phys. Chem. Chem. Phys. **1**, 1359 (1999).

[32] G. J. Kroes, Prog. Surf. Sci. **60**, 1 (1999).

[33] D. A. McCormack, G. J. Kroes, R. A. Olsen, I. A. Groeneveld, J. N. P. van Stralen, E. J. Baerends, and R. C. Mowrey, Faraday Discuss. **117**, 109 (2000).

[34] E. Pijper, M. F. Somers, G. J. Kroes, R. A. Olsen, E. J. Baerends, H. F. Busnengo, A. Salin, and D. Lemoine, Chem. Phys. Lett **347**, 277 (2001).

[35] P. Riviere, H. F. Busnengo, and F. Martín, J. Chem. Phys. **123**, 074705 (2005).

[36] G. J. Kroes and M. F. Somers, J. Theor. Comput. Chem. **4**, 493 (2005).

[37] C. Díaz, J. K. Vincent, G. P. Krishnamohan, R. A. Olsen, G. J. Kroes, K. Honkala, and J. K. Nørskov, Phys. Rev. Lett. **96**, 096102 (2006).

[38] W. C. Swope, H. C. Andersen, P. H. Berens, and K. R. Wilson, J. Chem. Phys. **76**, 637 (1982).

[39] R. Kosloff, J. Phys. Chem. **92**, 2087 (1988).

[40] J. C. Light, I. P. Hamilton, and J. V. Lill, J. Chem. Phys. **82**, 1400 (1985).

[41] M. D. Feit, J. A. Fleck, and A. Steiger, J. Comput. Phys. **47**, 412 (1982).

[42] D. Kosloff and R. Kosloff, J. Comput. Phys. **52**, 35 (1983).

[43] G. C. Corey and D. Lemoine, J. Chem. Phys. **97**, 4115 (1992).

[44] D. Lemoine, J. Chem. Phys. **101**, 10526 (1994).

[45] G. G. Balint-Kurti, R. N. Dixon, and C. C. Marston, J. Chem. Soc., Faraday Trans. **86**, 1741 (1990).

[46] E. Pijper, G. J. Kroes, R. A. Olsen, and E. J. Baerends, J. Chem. Phys. **117**, 5885 (2002).

[47] D. Neuhauser and M. Baer, J. Chem. Phys. **91**, 4651 (1989).

[48] A. Vibok and G. G. Balint-Kurti, J. Phys. Chem. **96**, 8712 (1992).

[49] K. D. Rendulic, G. Anger, and A. Winkler, Surf. Sci. **208**, 404 (1989).

[50] D. J. Auerbach, in *Atomic and molecular beam methods*, edited by G. Scoles (Oxford University Press, 1988), pp. 362–379.

[51] H. A. Michelsen and D. J. Auerbach, J. Chem. Phys. **94**, 7502 (1991).

[52] G. Herzberg, *Molecular spectra and molecular structure I. Spectra of diatomic molecules* (D. van Nostrand Company, Inc., Princeton, 1950).

[53] A. Gross, S. Wilke, and M. Scheffler, Surf. Sci. **357**, 614 (1996).

[54] C. T. Rettner, H. A. Michelsen, and D. A. Auerbach, J. Chem. Phys. **102**, 4625 (1995).

[55] J. Q. Dai and J. C. Light, J. Chem. Phys. **108**, 7816 (1998).

[56] A. Gross, S. Wilke, and M. Scheffler, Phys. Rev. Lett. **75**, 2718 (1995).

[57] D. Wetzig, R. Dopheide, M. Rutkowski, R. David, and H. Zacharias, Phys. Rev. Lett. **76**, 463 (1996).

[58] D. A. McCormack, G. J. Kroes, R. A. Olsen, E. J. Baerends, and R. C. Mowrey, J. Chem. Phys. **110**, 7008 (1999).

[59] J. Q. Dai and J. C. Light, J. Chem. Phys. **107**, 1676 (1997).

[60] H. Hou, S. J. Gulding, C. T. Rettner, A. M. Wodtke, and D. J. Auerbach, Science **277**, 80 (1997).

[61] E. Pijper, G. J. Kroes, R. A. Olsen, and E. J. Baerends, J. Chem. Phys. **113**, 8300 (2000).

[62] A. Gross and M. Scheffler, Chem. Phys. Lett **256**, 417 (1996).

[63] Y. Zhao and D. G. Truhlar, J. Chem. Phys. **128**, 184109 (2008).